# D3.4
# Optimised transducer design (final generation)

| General information | |
|---|---|
| Grant agreement number | 755500 |
| Start date of the project | 01/09/2017 |
| Project duration | 54 months |
| Due date of the deliverable | 30/04/2021 |
| Actual submission date | 21/02/2022 |
| Lead beneficiary | 6 – UoB |


| Keywords |
|---|
| Ultrasonic arrays, signal-to-noise ratio, multiple scattering |


| Type | Meaning | |
|---|---|---|
| R | Document, report | |
| DEM | Demonstrator, pilot, prototype | x |
| DEC | Websites, patent fillings, videos, etc. | |
| OTHER | Software, technical diagram, etc. | |

| Dissemination Level | | |
|---|---|---|
| PU | Public | x |
| CO | Confidential, only for members of the consortium (including the Commission Services) | |

# Table of Content

# Table of Tables



# Table of Figures



# GLOSSARY

| Abbreviations/Acronym | Description |
|---|---|
| **FOM** | Figure of Merit |
| **PSF** | Point Spread Function |
| **RMS** | Root Mean Square |
| **SDH** | Side Drilled Hole |
| **SNR** | Signal-to-Noise Ratio |

# 1 Summary

Imaging and defect detection in polycrystalline materials is a topic of significant interest and practical importance in non-destructive evaluation (NDE). Among many different inspection modalities ultrasonic testing is one of the most commonly applied methods because of the relatively low cost, good penetration depth, inspection speed, and portability. Recent advances in ultrasonic imaging have been based on the use of phased arrays. The concept of Full Matrix Capture (FMC), which consists of recording signals from all transmitter-receiver array elements, has completely transformed the use of ultrasonic arrays for NDE. This approach led to the development of many advanced signal processing algorithms, for example, multi-modal imaging and sub-wavelength defect characterisation methods. Although the basic principles of ultrasonic array imaging are now well established, the problem of optimising the parameters of ultrasonic array system for defect detection and characterisation in coarse grained materials remains open. This is a key motivation for the current work. In this report a general model for grain scattering noise in ultrasonic array images is developed, which includes both single and multiple scattering components and is used to quantitatively analyse the array imaging performance. The model allows to formulate quantitative guidelines that relate the image SNR to array system parameters. The results are illustrated on simulated and experimental data.

  

# 2 Introduction

In this report, the problem of optimising the parameters of an ultrasonic array system for inspection of coarse grained materials is considered. One common method of evaluating the limits of the inspection is with the use of probability of detection curves, calculated using large numbers of experimental results on many samples with artificially manufactured defects, all at a great cost. On the other hand, measuring backscattered signals from defect-free samples can be easily performed in an industrial setting and such samples are relatively cheap. This fact led to the development of an efficient modeling technique, which combines a simulated defect response with experimentally measured structural noise [1,2]. It has been demonstrated that this approach gives accurate results for the full range of signal-to-noise ratio (SNR), where meaningful data can be drawn from the image. Alternatively, the full complexity of the scattering phenomena can be taken into account by using numerical techniques, such as finite element (FE) methods. The most significant advancement has been in the utilization of graphics processing units (GPUs), which have been shown to reduce the processing time by 1–2 orders of magnitude [3,4].

However, the assessment of the array imaging performance using all mentioned methods can be performed only for some particular array configurations and defect types and sizes. Critically, these approaches cannot provide the full understanding of the relative importance of different physical factors and array parameters affecting the signal-to-noise (SNR) behaviour. The difficulty of inspecting polycrystalline materials is explained by the phenomenon of the ultrasonic wave scattering from grain boundaries. This interaction produces a backscattered signal which manifests itself as a speckle pattern on the ultrasonic array image and makes defect detection challenging. The scattering response consists of single and multiple scattering contributions. In single scattering, the main assumption is that the incident wave is only scattered by one local material scatterer. In this case the analysis of scattered signals allows an analytical treatment, and it has been extensively studied by many researchers. In the contexts of the inspection optimisation two important results must be mentioned. Firstly, Thompson and co-workers developed and validated single scattering models (using the Born approximation) of grain noise in aero-engine materials inspected using conventional ultrasonic single-element probes [5]. Secondly, Wilcox generalised this approach for predicting the SNR in a phased array image [6], which was then applied for comparison of ultrasonic array imaging algorithms in highly scattering materials [7].

However, it is well understood that the underlying physical reason for the detection limit corresponds to the increase of the multiple scattering contribution (when absorption losses are small). In multiple scattering, the signal is scattered many times between different scatterers. This process is much more complex compared to the single scattering case, and is usually modelled by applying various approximations, or by using numerical techniques. The fundamental difficulty in predicting the imaging performance is that the measured signal represents a combination of single and multiple scattered waves. Therefore, in general, apart from the limiting cases of dominant single and dominant multiple scattering, the single and multiple scattering effects cannot be studied separately.

Recently it has been shown that the relative proportion of the multiple scattering in an ultrasonic array image intensity (reffered to as a multiple scattering rate) can be measured from the FMC array data [8]. This development opens the possibility to use multiple scattering rate as a function of frequency and imaging depth as an optimisation tool for ultrasonic array inspection. In this work, a general model for grain scattering noise in ultrasonic array images is developed, which includes both single and multiple scattering components and is used to quantitatively analyse the array imaging performance. The model allows to

  

formulate quantitative guidelines that relate the image SNR to array system parameters. The results are illustrated on simulated and experimental data.

# 3 Measurement configuration

## 3.1 Test samples

In this paper, 2-D imaging using a 1-D linear ultrasonic array is considered. The measurements were conducted in direct contact configuration, and Cartesian coordinate axes $(x, z)$ are defined with the $z$ axis normal to the array (see Fig. 1a). For all examples the array data were acquired using the Full Matrix Capture (FMC) procedure and represent a dataset of all possible transmitter-receiver signals. Firstly, experimental array measurements were performed on the copper and Inconel 600 (1618-B359-B3) samples. Note, that for the Inconel sample the grain size distribution has been thoroughly studied with micrographic analyses as well as EBSD, however, metallographic characterisation of the copper sample was not performed. In addition, a Finite Element (FE) method was used to simulate array signals scattered by a grain structure, and the material properties corresponding to copper were chosen as $c_{11}$ = 168.6 GPa, $c_{12}$ = 121.4 GPa, $c_{44}$ = 75.4 GPa, and $\rho$ = 8960 kg/m$^3$ ($c_{11}$, $c_{12}$, and $c_{44}$ are elastic constants of a cubic material). Pogo software package [3] was chosen as the FE solver. A detailed description of the modelling procedure can be found in [2]. The first group of measurements was taken on the defect free part of each sample in order to measure the grain scattering data only. The second set of FMC array data was collected for side drilled holes of different diameters located directly below array center. Parameters of material samples and ultrasonic arrays used to make measurements are listed in Tables 1 and 2, respectively.

Measurements from defect-free regions were used to estimate an ultrasonic attenuation and longitudinal velocity for each sample. The measured A-scan signal was averaged over all trasmitter-receiver pairs (this corresponds to the equivalent pulse-echo signal obtained with an unfocused monolithic transducer), and then relative amplitude and arrival time of the first and second backwall reflections give the attenuation coefficient and the ultrasonic velocity for the considered medium. In this case, no correction for the beam spread effect was applied as for the considered array apertures and sample depths this was shown to have negligible effect [1,2]. It was found that over array bandwidth the attenuation coefficient as a function of frequency follows the power law, $\alpha = cf^n$, where material parameters *c* and *n* are given in Table 1. Note, that measured values of power exponent *n* were very close to an integer, and so the rounded integer values were used for the calculations in the rest of the report (see also discussion in [9]).

| Sample label | Material | Depth (mm) | Average grain size / standard deviation (µm) | Velocity (m/s) | Attenuation | | Number of defect free measurements | Defects |
|---|---|---|---|---|---|---|---|---|
| | | | | | n | c, $\frac{(\mu s)^n}{m}$ | | |
| A | Copper | 65 | - | 4800 | 2 | 2.8 | 8 | 1 mm SDH at 40 mm |
| B | Inconel | 90 | 740 / 400 | 5844 | 2 | 3.8 | 6 | 2 mm SDH at 40, 60 mm |
| C | Copper, 2D FE model | 40 | 100 / 100 | 4690 | 3 | 0.7 | 30 | 2, 0.12 mm SDHs at 20 mm |

**Table 1: Sample specifications used in experiments and modelling.**

| Sample label | Number of Elements | Central Frequency (MHz) | Element | | |
|---|---|---|---|---|---|
| | | | Width (mm) | Pitch (mm) | Length (mm) |
| A | 64 | 5 | 0.53 | 0.63 | 15 |
| B | 64 | 2 | 1.32 | 1.57 | 22 |
| C | 64 | 2.5 | 0.35 | 0.5 | - |

**Table 2**: Array transducer specifications used in experiments and modelling.

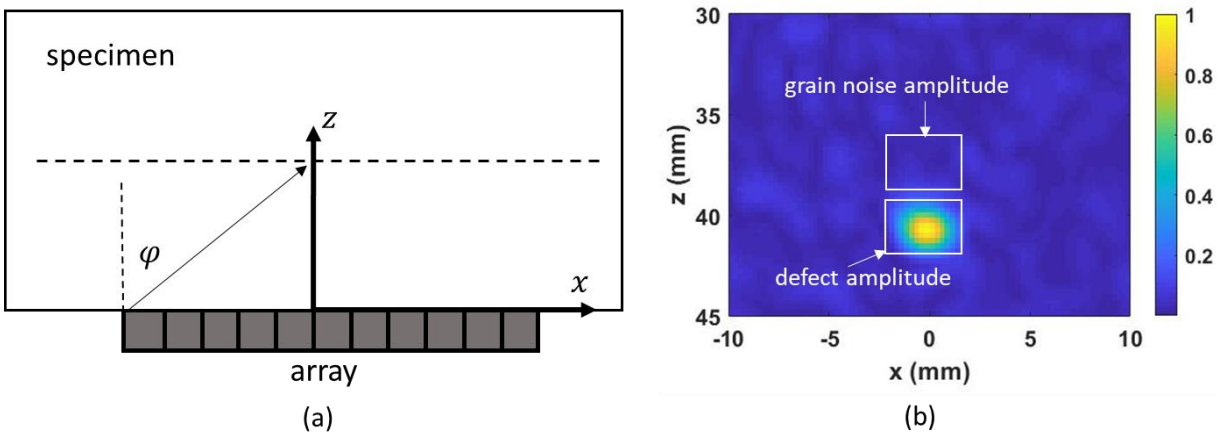


**Figure 1: (a) Array measurement geometry; (b) Image of 1 mm SDH in the copper sample at 3 MHz, $\varphi = 20^0$.**

## 3.2 Defect scattering matrix

The scattering behaviour of a defect can be characterised by its scattering coefficient matrix [10], which represents defect's scattering directivity pattern for a given incident plane wave. In a general 3D case, for a unit amplitude incident plane wave and a defect located at $\{x_0, y_0, z_0\}$, the frequency spectrum of the scattered wave at the location $\{x, y, z\}$ can be written in terms of the angular spectrum, $U_{3D}$, as [11,12]

$$u_{sc} = \frac{1}{4\pi^2} \iint U_{3D}(k_x, k_y) e^{i\boldsymbol{kr}} dk_x dk_y, \tag{1}$$

where $\boldsymbol{k} = \{k_x, k_y, k_z\}$ is the wavevector and $\boldsymbol{r} = \{x - x_0, y - y_0, z - z_0\}$. In the far-field integral (1) can be evaluated using the stationary phase method as

$$u_{sc} = \frac{1}{r} S_{3D} e^{ikr}. \tag{2}$$

The scattering matrix $S_{3D}$ is related to the angular spectrum by [11,12]

$$S_{3D} = \frac{ik}{2\pi} \cos\varphi \, U_{3D}, \tag{3}$$

where $\varphi$ is the scattering angle, corresponding to the elevation angle in 3D case (see Fig.1). For 1D array oriented along $x$-axis, the scattered wave field has to be integrated along $y$-direction. Therefore, the far-field expression becomes

$$u_{sc} = \frac{1}{\sqrt{r}} S_{2D} e^{ikr}. \tag{4}$$

Here 2D scattering matrix, $S_{2D}$, is defined as

  

$$S_{2D} = e^{-\frac{i\pi}{4}} \left(\frac{k}{2\pi}\right)^{\frac{1}{2}} \cos\varphi \, U_{2D}, \tag{5}$$

where $U_{2D}(k_x) = U_{3D}(k_x, 0)$. Finally, from expressions (3) and (5) the following relationship between 3D and 2D scattering matrices can be obtained:

$$S_{3D} = e^{i3\pi/4} \left(\frac{k}{2\pi}\right)^{\frac{1}{2}} S_{2D}. \tag{6}$$

# 4 Signal-to-noise ratio

## 4.1 Preliminary considirations

The majority of array imaging methods are based on the single scattering assumption and effectively focus the scattered signals back to the scatterer location. In this case the multiple scattering contribution acts as a noise, and is the main reason for the image quality degradation at high frequencies and large imaging depths. In this report the back-propagation imaging method [11] is used for data processing. However, it was shown that the backpropagation method and other well-known linear imaging methods are closely related to each other and can all be expressed in the delay and sum form [12]. It means that all results obtained here are also directly applicable to other linear imaging algorithms.

The array imaging performance is mostly affected by two main parameters: an aperture angle (described by the angle $\varphi$ in Fig. 1a), and a frequency. The aperture angle can be controlled by an angular filter, which represents a binary weighting factor applied to the image contributions from array elements [13]. Similarly, the imaging frequency is controlled by applying a frequency filter to the FMC data, which are then converted into corresponding images. In this work, a Gaussian filter with the center frequency $f$ and a half bandwidth $0.5f$ is chosen. This ensures that the resolution in the $z$-direction in terms of wavelength is the same at all frequencies.

The defect's detectability is usually characterised by the signal-to-noise ratio, $\delta_{snr}(z, f, \varphi)$, where $z$ is the defect's depth. The signal is defined as the maximum image amplitude of the defect. The appropriate noise measure is the root mean square (RMS) of the grain noise image amplitude. Ideally, the grain noise should be measured at the same location as the defect. In practice this will require defect free reference samples and careful calibration, which makes the SNR measurement procedure complicated. Alternatively, the SNR can be measured from the same image containing the defect. In this case the noise area must be chosen away from the defect position. However, if the image region is located at a different lateral position compared to the defect, then it might have a different angular coverage. On the other hand, the image region located below the defect is affected by the defect's shadowing. Therefore, in this work the grain noise was measured in the area located at the same lateral position, but above the defect at $z_n < z$ as shown in Fig. 1b, resulting in a slightly different SNR value, $\delta'_{snr}(z, z_n)$. However, it will be shown that there is a direct relationship between $\delta_{snr}$ and $\delta'_{snr}$, which can be used to calculate $\delta_{snr}$.

A detection threshold is needed to determine the existence of a defect. It is assumed that the grain noise image amplitude follows a Rayleigh distribution. If there are $N$ independent pixels in the considered image area, then the probability of false alarm, $p_{fa}$, is given by

$$p_{fa} = 1 - \left(1 - e^{-\delta_{snr}^2}\right)^N. \tag{7}$$

If $p_{fa} \ll 1$, then the required threshold can be estimated as

$$\delta_{snr} = \sqrt{\ln \frac{N}{p_{fa}}}. \tag{8}$$

In the examples considered in this report $N \sim 100$ and the false alarm rate is set to $p_{fa} = 10^{-3}$, therefore the detection threshold is 3.4 or 10.6 dB.

In terms of image intensities (square of the image amplitude), SNR can be written as

$$\delta_{snr} = \left(\frac{I_{max}}{I}\right)^{1/2}, \tag{9}$$

  

where $I_{max}$ is the maximum defect image intensity, and $I$ is the average grain scattering image intensity. In a random scattering medium the total image intensity can be written as a sum of single and multiple scattering intensities, $I = I_S + I_M$. Then expression (9) for the SNR can be rearranged in order to separate single and multiple scattering effects:

$$\delta_{snr} = \delta_{snr,S}\, \delta_S^{1/2}, \tag{10}$$

where the single scattering signal-to-noise ratio, $\delta_{snr,S}$, and the single scattering rate, $\delta_S$, are defined as

$$\delta_{snr,S} = \left(\frac{I_{max}}{I_S}\right)^{\frac{1}{2}}, \qquad \delta_S = \frac{I_S}{I}. \tag{11}$$

## 4.2 Single scattering

In the single scattering case it was shown that the general expression for the signal-to-noise ratio is given by [6]

$$\delta_{snr,S} = \frac{A_s}{A_n} \frac{1}{\sqrt{\int |P|^2 d\boldsymbol{r}}}. \tag{12}$$

Here $A_s$ is the scattering amplitude of the defect and $P$ is the normalised point spread function (PSF), $P(0) = 1$. Note that for a 3D grain structure (as in experimental examples) the PSF in expression (12) corresponds to the 3D point scatterer, although the imaging is performed by 1D array. Then $A_n$ is the square root of the backscattering coefficient, or the grain noise Figure of Merit (FOM) [14-16], which is related to the number of grains per unit volume and the average single grain backscattering coefficient. In the particular case of equiaxed grains with the average size $d$ (which is defined here as the correlation length corresponding to the two-point correlation function [17]), the FOM can be written as

$$A_n = C_n \tilde{A}_n / \sqrt{d}, \tag{13}$$

where $C_n$ is the material constant, and the normalized Figure of Merit, $\tilde{A}_n$, is given by

$$\tilde{A}_n = \begin{cases} \left[\dfrac{(kd)^2}{1+(kd)^2}\right]^{3/4}, & 2D\ (FE\ model) \\ \dfrac{(kd)^2}{1+(kd)^2}, & 3D. \end{cases} \tag{14}$$

The defect's scattering amplitude, $A_s$, is directly related to the defect's scattering matrix, $S$, as

$$A_s = C_s \tilde{A}_s, \quad \tilde{A}_s = k^{\beta} S, \tag{15}$$

where $C_s$ is a constant. Expressions for the normalized scattering amplitude, $\tilde{A}_s$, for 1D array imaging and different scatterer types can be obtained from the results of section 3.2 and are given in Table 3. Note, that for simplicity it is assumed that scattering coefficients $A_n$ and $A_s$ weakly depend on the incident and scattered angles within the array angular aperture, which is a reasonable approximation for the cases considered in this report.

The lateral size of the PSF is inversely proportional to the maximum lateral wavenumber component, and its axial size is proportional to the initial pulse length. Therefore, the integral in (12) can be written as

$$\int |P|^2 d\boldsymbol{r} = C_p (f^2 \sin\varphi)^{-1}, \tag{16}$$

where $C_p$ is a constant, which depends on the type of the imaging algorithm. Finally, the single scattering SNR as a function of angular aperture and frequency can be written in the following form:

  

$$\delta_{snr,S}(\varphi, f) = C_\delta \frac{\tilde{A}_s}{\tilde{A}_n} f\sqrt{\sin\varphi}, \tag{17}$$

here $C_\delta = C_s C_p^{-1/2} C_n^{-1}\sqrt{d}$ .

| Scatterer type | $\tilde{A}_s$ | |
|---|---|---|
| | 2D (FE model) | 3D |
| 2D scatterer | $S_{2D}$ | $S_{2D}\sqrt{k}$ |
| 3D scatterer | - | $S_{3D}$ |
| Back wall | $1/\sqrt{k}$ | 1 |

**Table 3: Relationships between scattering amplitude and scattering matrix for different scatterer types.**

## 4.3 Multiple scattering

Expression (17) shows that under the single scattering assumption SNR increases as the imaging frequency increases. However, multiple scattering is always present and is the primary cause of the severe performance limitations at high inspection depths and frequencies. Therefore, it is important to estimate the amount of the multiple scattering contribution and take it into account in the general SNR model. Multiple scattering can be characterized by its reciprocal quantity, the single scattering rate, which is defined as a proportion of the single scattering contribution in the total image intensity. It was shown that the single scattering rate can be estimated directly from the array image [8]. Figs.2a, 3a, 4a show the single scattering rate as a function of depth and frequency for the numerical and two experimental examples considered in the report. Note that the single scattering rate is closely related to the scattering attenuation, because the physical origin of these two phenomena is the same. It was empirically found that an adequate approximation to the single scattering rate, similarly to the coherent attenuation, can be described by the exponential function as

$$\delta_S(\varphi, f, z) = e^{-2\alpha_s z}, \;\; \alpha_s = c_s(\varphi) f^n, \tag{18}$$

where the power exponent $n$ is the same as for the attenuation coefficient $\alpha$ (Table 1). Exponential fits, corresponding to the directly measured single scattering rates, are shown in Figs.2b,3b,4b, and a good agreement is demonstrated. Note, that because of empirical nature of relationship (18), its validity domain (outside of the measured frequency range) is not exactly known. This question requires separate detailed investigation, which is beyond of the scope of this work. The coefficient $c_s$ as a function of the angular aperture $\varphi$ is shown in Figs.2c,3c,4c (the value $c$ in these figures corresponds to the plane wave attenuation, see Table 1). It can be seen that in the range $10^0 \le \varphi \le 30^0$ the coefficient $c_s$ (and therefore, the single scattering rate) is almost independent on the aperture angle and

$$\alpha \le \alpha_s \le 2\alpha. \tag{19}$$

It is interesting to note that for two experimental samples $\alpha_s$ is very close to $\alpha$, but for FE simulations $\alpha_s$ is close to $2\alpha$. This difference is thought to be caused by the grain structure dimentionality, which is 3D in real samples and 2D in FE model. Importantly, this observation highlights the fact, that there are significant fundamental differences between 2D and 3D scattering, and 2D simulations can not be considered as fully representative of real 3D microstructures. In this context the paper [9] must also be mentioned, where the frequency dependence of the coherent attenuation $\alpha$ was analysed using 2D and 3D FE simulations.

  

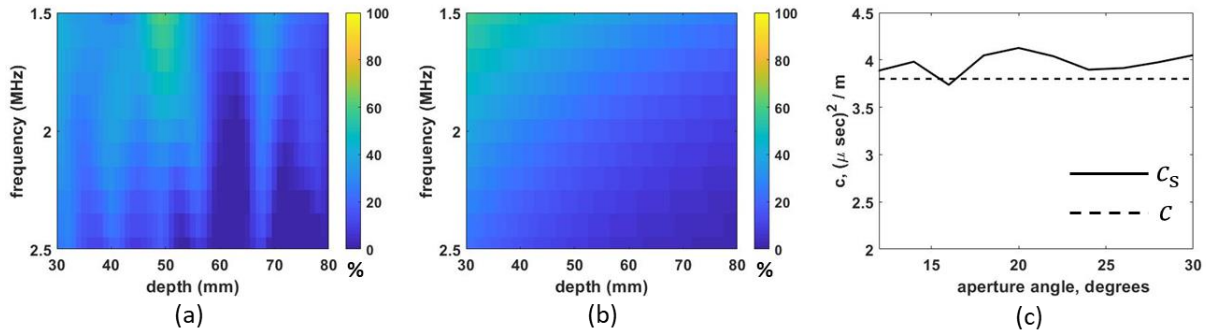


**Figure 2: Single scattering rate for the inconel sample, experiment (a) and exponential fit (b), $\varphi = 20^0$; (c) coefficient $c_s$.**

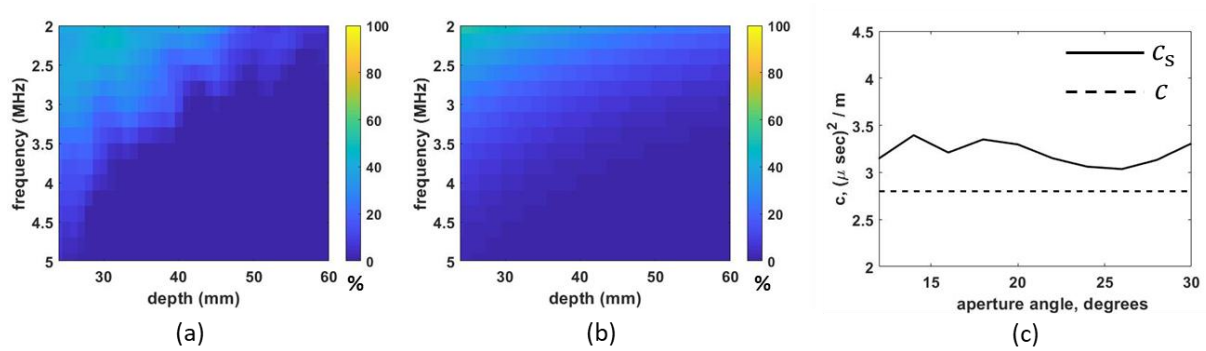


**Figure 3: Single scattering rate for the copper sample, experiment (a) and exponential fit (b), $\varphi = 20^0$; (c) coefficient $c_s$.**

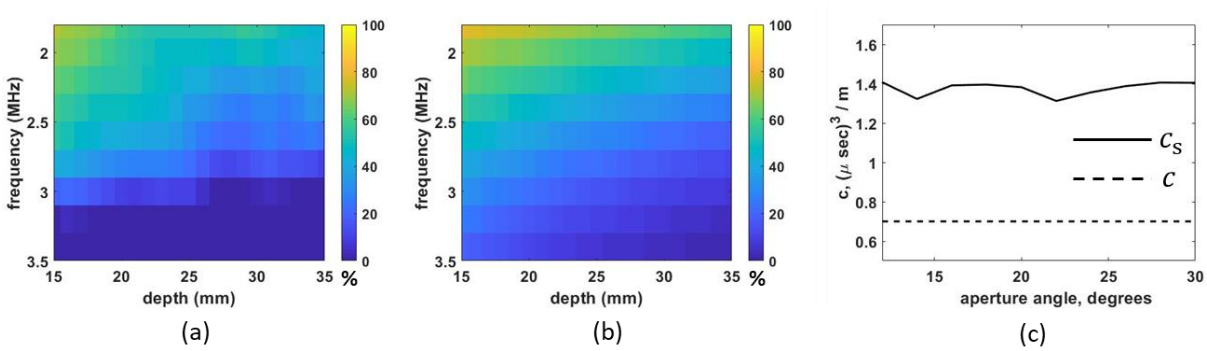


**Figure 4: Single scattering rate for the copper sample, 2D FE model, experiment (a) and exponential fit (b), $\varphi = 20^0$; (c) coefficient $c_s$.**

## 4.4 General model

Combining results in sections 4.1, 4.2 and 4.3, the following expression for the SNR can be obtained:

$$\delta_{snr} = C_\delta \frac{\tilde{A}_s}{\tilde{A}_n} f e^{-\alpha_s z} \sqrt{\sin\varphi}. \tag{20}$$

Note that in expression (20) it is assumed that the signal and noise amplitudes are measured at the same depth $z$. Therefore, although both signal and noise are affected by the attenuation, $\tilde{A}_s, \tilde{A}_n \sim \exp(-2\alpha z)$, their ratio does not explicitly depend on the attenuation. However, as it was explained in section 4.1, in practice it is more convenient to measure the noise at different depth, $z_n < z$. In this case the signal-to-noise ratio, $\delta'_{snr}(z, z_n)$, is related to $\delta_{snr}$ as

$$\delta'_{snr}(z, z_n) = \delta_{snr} e^{-(2\alpha - \alpha_s)(z - z_n)}. \tag{21}$$

In general, the scaling coefficient $C_\delta$ in (20) depends on material properties. However, it can be calculated by measuring the signal-to-noise ratio, $\delta_{snr}^{ref}(z_{ref})$, of some reference scatterer (for example, a back wall), located at $z_{ref}$. Then the SNR of a defect located at $z$, is given by

$$\delta_{snr}(z) = \delta_{snr}^{ref}(z_{ref}) A_s^{ref} e^{-\alpha_s(z-z_{ref})}, \tag{22}$$

where $A_s^{ref}$ is the defect image amplitude relative to the reference scatterer.

  

# 5 Validation

## 5.1 Average grain size estimation

One application of model (20) is to predict the SNR of a defect of interest and to find optimal array inspection parameters, which is the main focus of this report. Alternatively, it can also be used to estimate the grain noise Figure of Merit $A_n$, which incorporates material microstructural properties, in particular the average grain size $d$. Fig.5 shows the normalized FOM as a function of the normalized frequency $kd$. It can be seen that at low frequencies $\tilde{A}_n \sim (kd)^2$, and at high frequencies $\tilde{A}_n \sim 1$. Note that conventional backscatterer methods of material characterization [18,19] are based on the single scattering assumption, which is valid at low frequencies when the wavelength is large compared to the grain size, $kd \ll 1$. In this case the FOM $A_n = C_n d^{3/2} k^2$, so material parameters $C_n$ and $d$ are combined into one scaling factor, and in order to obtain $d$ the material constant $C_n$ must be known. Importantly, expression (20) is valid for all frequencies, and, therefore, allows to measure the FOM even in the dominant multiple scattering regime, $kd \geq 1$. Note, that in the intermediate frequency regime, $0.5 \leq kd \leq 4$, parameters $C_n$ and $d$ are not coupled in the expression for $A_n$, and, therefore, can be found independently by fitting the model (13)-(14) to the measured FOM.

Results of the grain size estimation for the Inconel sample are presented in Figs.6a,b. The side drilled hole (SDH) of 2 mm diameter located at 40 mm depth was used as a reference scatterer. Firstly, for each value of $d$ the constant $C_n$ was found from the best linear fit. Fig.6a shows the relative residual fitting error of the normalised FOM as a function of the parameter $d$. Then the average grain size was defined as a value of $d$, corresponding to the smallest fitting error. It is seen that the estimated grain size is about 650 µm, which is in the good agreement with the metallographic measurements of 740 µm (see Table 1).

Figs.6c-f show the results for the copper sample. In this case the grain size was not known, and SNR measurements for two reference scatterers were used. The first scatterer was a 1 mm SDH located at 40 mm depth, and the back wall at the defect free part of the sample with 40 mm depth was used as the second reference scatterer. It can be seen that in both cases the mean grain size was estimated as $d \approx 200$ µm.

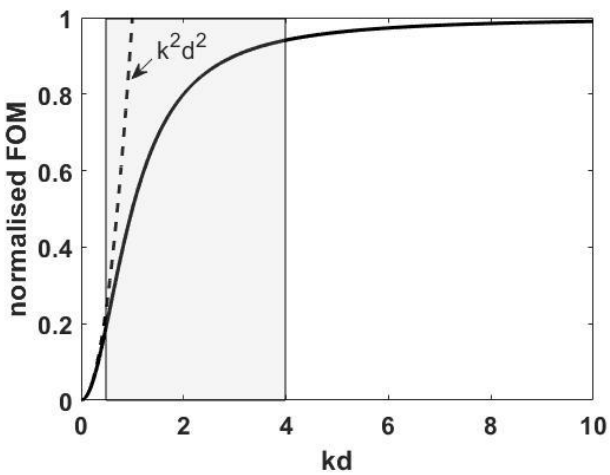


**Figure 5: Normalised Figure of Merit (expression (14))**

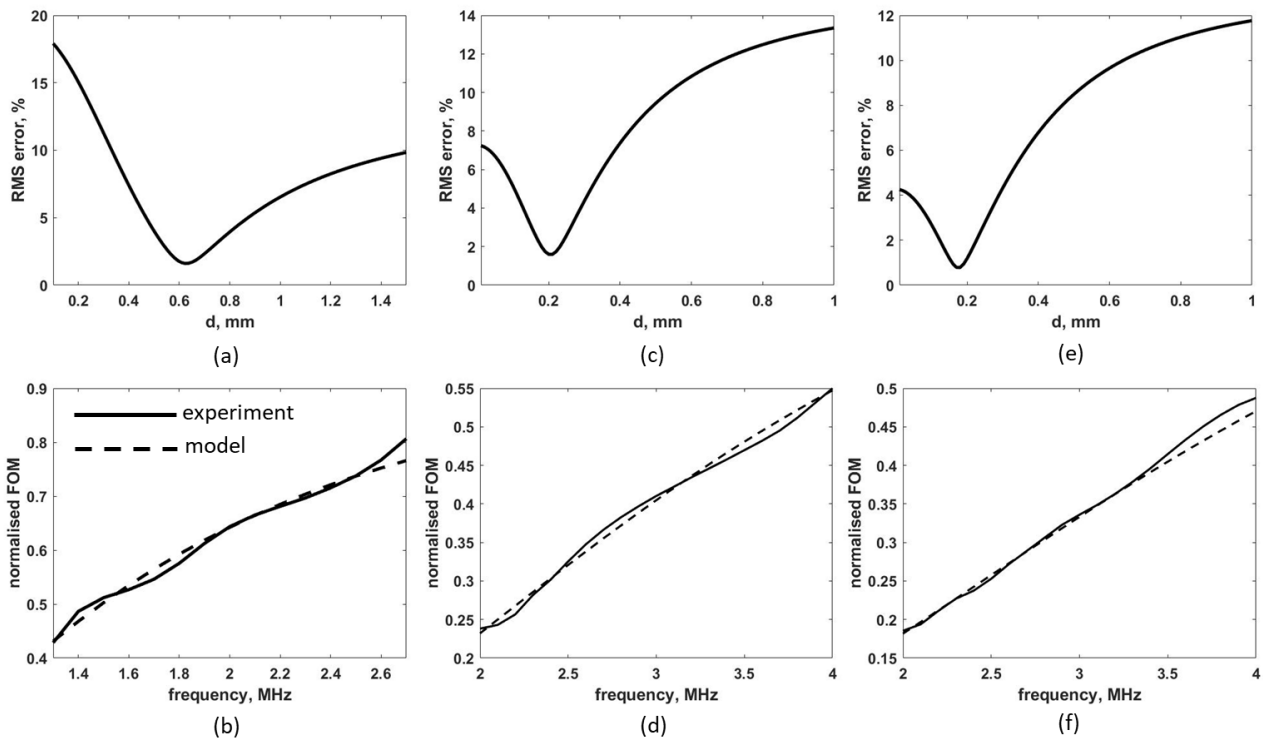


**Figure 6: Results of the average grain size estimation. Top row: relative RMS fitting error of the normalised FOM as a function of the grain size. Bottom row: Measured and modelled normalised FOM. (a), (b) Inconel sample, 2 mm SDH at 40 mm depth; (c), (d) Copper sample, 1 mm SDH at 40 mm depth; (e), (f) Copper sample, back wall at 40 mm depth.**

## 5.2 Image intensity

Another application of the developed SNR model is to predict the array image intensity variation as a function of depth and frequency. As it follows from expression (21), the image intensity $I$ can be written as

$$I(z,f) = C_I e^{-2(2\alpha-\alpha_s)z} \,. \tag{22}$$

From (19) and expression (22) it can be seen that $I \sim \exp\,(-2c_\alpha \alpha z)$, where the coefficient $0 \leq c_\alpha \leq 1$. The important conclusion is that the image intensity decrease rate is slower than that given by the single scattering model with the plane wave coherent attenuation coefficient, $I \sim \exp\,(-4\alpha z)$. Physically this is explained by the multiple scattering contribution to the total image intensity. Interestingly, this effect is independent of frequency and present even at low frequencies in the dominant single scattering regime. These conclusions are supported by experimental measurements, presented in Fig.7. Note that the same effect, but related to the backscattered time-domain signal amplitude attenuation, has been reported before in [20,21].

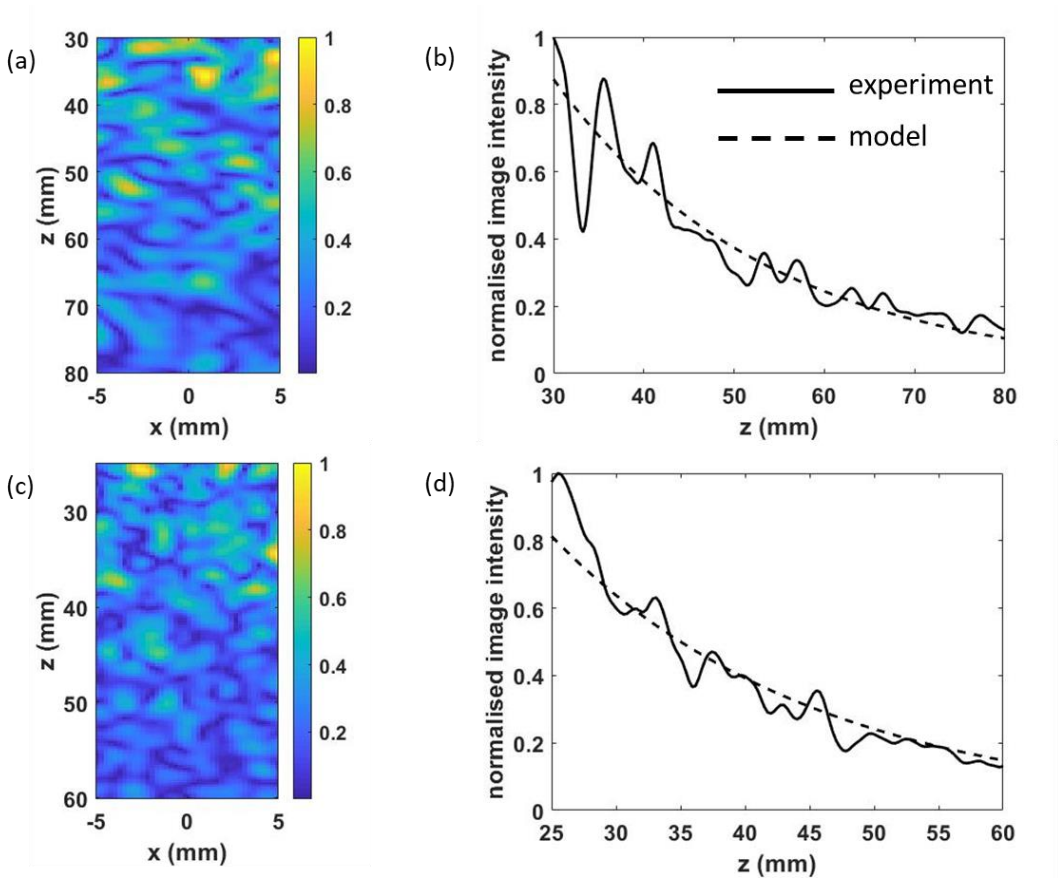


**Figure 7: Image intensity variation for Inconel, 2.5 MHz, $\varphi = 25^0$ (a,b) and Copper, 3 MHz, $\varphi = 20^0$ (c,d) samples. (a,c) array images; (b,d) average image intensity as a function of depth.**

## 5.3 Signal-to-noise ratio

Fig.8 compares the measured and modelled SNR as a function of the array aperture angle for different defects in Inconel and copper samples. Results for the SNR as a function of frequency are presented in Fig.9. Note that for experimental measurements on the copper sample the normalized FOM was calculated using the mean grain size $d = 200\ \mu m$, estimated in section 5.1. These results show an excellent agreement with the experimental and simulated data, and therefore provide a validation for the SNR model (20).

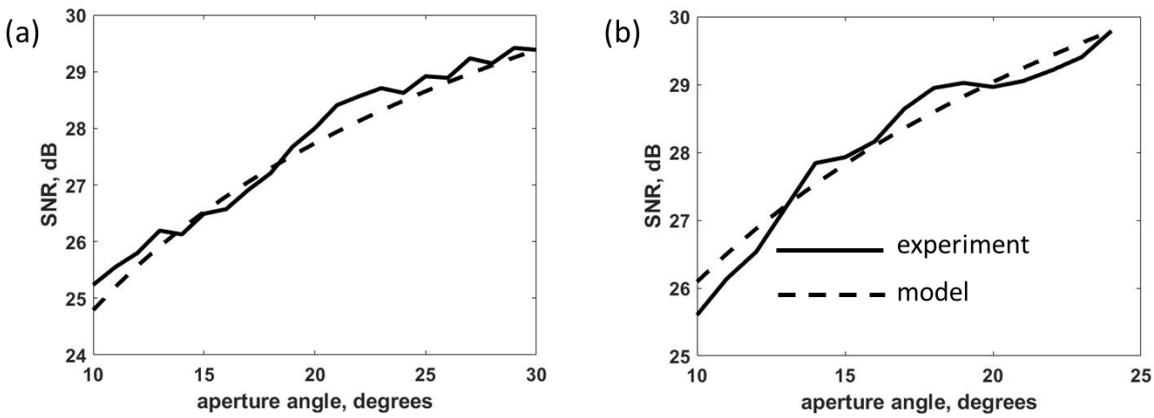


**Figure 8: SNR as a function of aperture angle for (a) 2 mm SDH at 40 mm depth in Inconel sample, *f* =2 MHz; (b) 1 mm SDH at 40 mm depth in Copper sample, *f* =3 MHz.**

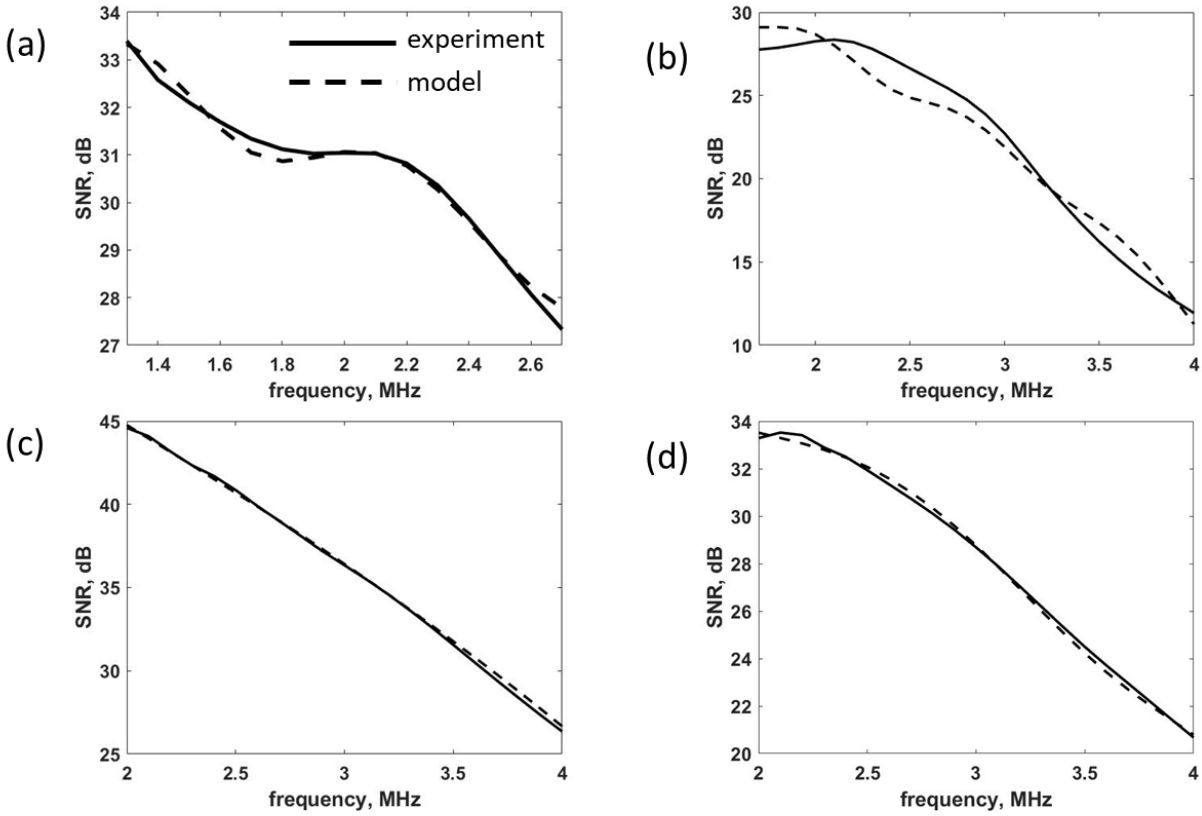


**Figure 9: SNR as a function of frequency for (a) 2 mm SDH at 40 mm depth in Inconel sample, $\varphi = 25^0$; (b) 2 mm SDH at 20 mm depth in Copper sample, 2D FE model, $\varphi = 20^0$ ; (c) 1 mm SDH at 40 mm depth in Copper sample, $\varphi = 20^0$; (d) back wall at 40 mm depth in Copper sample, $\varphi = 20^0$.**

# 6 Discussion

Expression (20) shows that the SNR is mainly influenced by two array system parameters: array aperture angle, $\varphi$, and imaging frequency, $f$. Firstly, the effect of the aperture angle is analysed. The dependence of the SNR on $\varphi$ is controlled by the single scattering attenuation coefficient $\alpha_s$ and the factor $\sqrt{\sin\varphi}$, which corresponds to the array focussing performance. However, the results of section 3.1 show that in the angular range $10^0 \leq \varphi \leq 30^0$, which is the most common in practical applications, the single scattering attenuation is almost completely independent of the aperture angle. In this case the SNR behaviour is primarily determined by the factor $\sqrt{\sin\varphi}$. Therefore, the expected improvement in SNR, which can be achieved by increasing the angular aperture from $10^0$ to $30^0$, is about 5 dB.

The imaging frequency has a much greater effect on the array imaging performance and therefore can be considered as the main optimisation parameter. The analysis of the experimentally measured SNR as a function of frequency is limited by the size of the array bandwidth. For example, as can be seen from Fig.9, the SNR monotonically decreases with the frequency in the measurable frequency range. However, from these data it is impossible to determine the defect's detection limit, as well as the point of the maximum sensitivity. In this case, model (20) provides the crucial tool, which can be used to analyse the SNR in a wide range of frequencies and to find the optimal performance point. It should be mentioned, that the SNR model (20)requires the knowledge of the single scattering rate as a function of frequency. In this work, empirical exponential expression (18) was found to provide a good approximation, and it was hypothesised that this expression remains valid in the considered frequency range (outside of the transducer bandwidth). Note, that the validity of this assumption is less important at low frequencies, where the contribution of multiple scattering is relatively small. However, in general this question requires a further detailed investigation, and it will be addressed in future work.

Fig. 10a shows the SNR for the 2 mm SDH located at 40 mm depth in the Inconel sample. The modelled SNR is plotted for the extended frequency range from 0.1 MHz to 5 MHz, which can be approximately splitted into three regions. The first region corresponds to low frequencies, $f \leq 1$ MHz, and the predominantly single scattering regime, $\delta_S \geq 70\%$, where the SNR follows the single scattering trend. The SNR behaviour in the dominant multiple scattering region, $f \geq 3$ MHz, $\delta_S \leq 5\%$ is determined by the single scattering exponential decay, $\delta_{snr} \sim f e^{-\alpha_s z}$. In the frequency range $5\% \leq \delta_S \leq 70\%$ the SNR exibits an intermediate behaviour. It can be seen that the detection limit corresponds to 4.9 MHz. On the other hand, the maximum sensitivity is achieved at 0.4 MHz. However, as the maximum SNR value is relatively high, it is possible to perform imaging at higher frequencies, which improves the image resolution, but keeps the SNR well above the detection threshold. Therefore, in this particular case the optimal performance point is likely to be at higher frequencies, $2\ \mathrm{MHz} \leq f \leq 4\ \mathrm{MHz}$, and represents a compromise between the image resolution and the required SNR level.

Fig. 10b shows the SNR as a function of frequency for a very small defect at the limit of array detectability. In this case the FE model was used to simulate array data for 0.12 mm SDH located at 20 mm depth in the copper sample C (see Table 1) and the SNR was averaged over 30 realizations of grain noise. It can be seen that there is an excellent agreement between the analytical model and the SNR measured from the FE data. The maximum sensitivity is achieved at $f \approx 2.4\ \mathrm{MHz}$, which corresponds to the intermediate frequency region, where $\delta_S \approx 45\%$ and the SNR behaviour is determined by both single and multiple scattering contributions. Importantly, in this case the maximum sensitivity point also represents the optimal imaging frequency.

  

The SNR model (20) can also be used to evaluate the array sensitivity to other possible defects, which can be difficult to manufacture in order to perform experimental measurements. As an example, the SNR for 3D spherical voids (porosity) located at 40 mm depth in the Inconel sample is presented in Fig. 11. It can be seen that as the size of a void decreases, the maximum sensitivity point is shifting from the single scattering region to the intermediate frequency region. The smallest detectable void is approximately 0.7 mm, which is comparable to the mean grain size. In this case the optimal inspection frequency is 2.7 MHz and corresponds to the onset of the dominant multiple scattering regime.

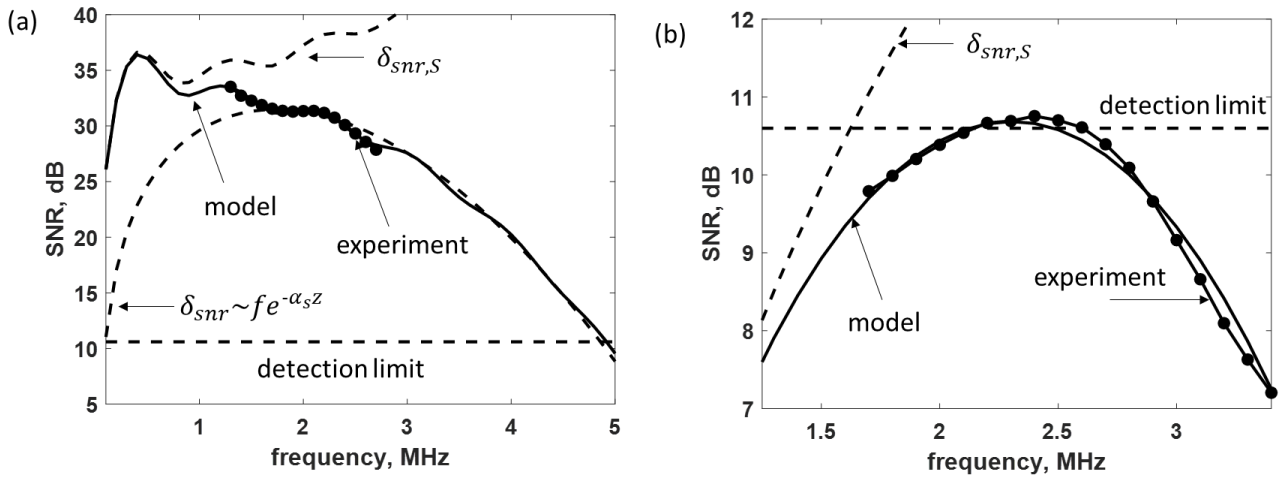


**Figure 10: SNR as a function of frequency for (a) 2 mm SDH at 40 mm depth in Inconel sample; (b) 0.12 mm SDH at 20 mm depth in Copper sample (FE model) .**

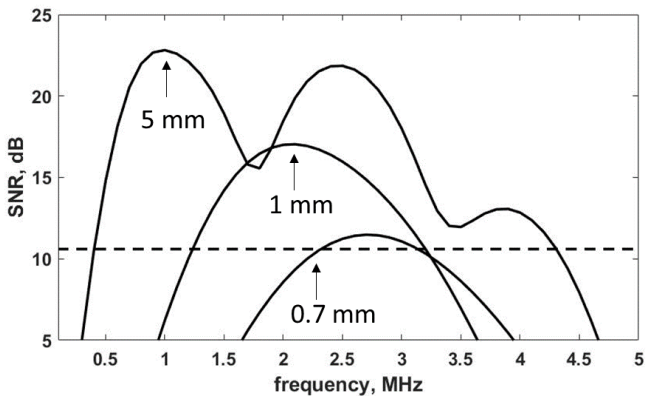


**Figure 11: SNR as a function of frequency for spherical voids of 5 mm, 1 mm and 0.7 mm diameter, located at 40 mm depth in Inconel sample.**

# 7 Conclusions

In this report the problem of finding optimal ultrasonic array parameters for imaging in materials with a high structural noise has been considered. In particular, the effects of array angular aperture and imaging frequency on the SNR have been analysed. In order to quantify the array performance, a general model of the SNR which includes single and multiple scattering contributions has been developed. Additionally, experimental measurements and FE simulations have been performed, and a good agreement has been found between the model predictions and measurement results.

The main conclusions can be summarised as follows.

- The multiple scattering effect in the SNR model is represented by an exponential factor, $e^{-\alpha_s z}$, which describes the proportion of the single scattering contribution in the total image amplitude. The single scattering attenuation coefficient $\alpha \leq \alpha_s \leq 2\alpha$, where $\alpha$ is the plane wave coherent atteniuation.
- The SNR model provides a tool to measure the material Figure of Merit even in the strongly multiple scattering regime. This makes it possible to estimate the mean grain size from the normalised FOM without independent measurement of material elastic constants.
- Multiple scattering has significant impact on the depth and frequency dependence of the image intensity, $I \sim e^{-2(2\alpha-\alpha_s)z}$. In particular, the image intensity attenuation rate is more than two times smaller than that given by the coherent attenuation $e^{-4\alpha z}$.
- SNR dependence on the array aperture angle in the range $10^0 \leq \varphi \leq 30^0$ is mainly determined by the array focussing effect and is described by the factor $\sqrt{\sin\varphi}$ .
- SNR frequency behaviour is characterised by three regions:
    - Low frequency region $f \leq f_S$, corresponding to the predominantly single scattering regime, where the single scattering rate $\delta_S \geq 70\%$. In this case the SNR variations are described by the single scattering model.
    - Intermediate region, $5\% \leq \delta_S \leq 70\%$.
    - Dominant multiple scattering regime, $\delta_S \leq 5\%$, where the SNR rapidly decreases because of the single scattering exponential decay factor.
- The SNR peak (point of the maximum sensitivity) is determined by the frequency behaviour of the defect's scattering coefficient (which is mainly governed by the defect size) and the multiple scattering effect (single scattering attenuation).
    - For relatively large defects, with the size comparable or larger than the wavelength at $f = f_S$, the point of maximum sensitivity is located in the single scattering region $f \leq f_S$, and is primarily determined by the single scattering factors.
    - For defects with the size smaller, than the wavelength at $f = f_S$, the point of maximum sensitivity is gradually shifting from the single scattering region to the intermediate frequency region, and is determined by the combined effect of single scattering and multiple scattering contributions.
    - In all cases, if the maximum SNR is close to the detection limit (for example, weak inclusions, small porosity, unfavourably oriented cracks or crack tip diffraction signal), then the optimal inspection frequency corresponds to the maximum sensitivity point. Otherwise, for stronger scattering defects, the optimal performance point is likely to be at higher frequencies and is defined by the compromise between the image resolution and the required SNR level.

# 8 Bibliography

[1] H. A. Bloxham, A. Velichko, and P. D. Wilcox, “Combining simulated and experimental data to simulate ultrasonic array data from defects in materials with high structural noise,” IEEE Trans. Ultrason., Ferroelectr., Freq. Control, vol. 63, no. 12, pp. 2198–2206, 2016.

[2] H. A. Bloxham, A. Velichko, and P. D. Wilcox, “Establishing the limits of validity of the superposition of experimental and analytical ultrasonic responses for simulating imaging data,” IEEE Trans. Ultrason., Ferroelectr., Freq. Control, vol. 66, no. 1, pp. 101–108, 2019.

[3] P. Huthwaite, “Accelerated finite element elastodynamic simulations using the GPU,” J. Comput. Phys., vol. 257, pp. 687–707, 2014.

[4] M. Huang, G. Sha, P. Huthwaite, S. I. Rokhlin, and M. J. S. Lowe, “Maximizing the accuracy of finite element simulation of elastic wave propagation in polycrystals”, J. Acoust. Soc. Am. 148 (4), pp.1890-1910, 2020.

[5] I. Yalda, F. J. Margetan, and R. B. Thompson, “ Predicting ultrasonic grain noise in polycrystals: A Monte Carlo model,” J. Acoust. Soc. Am. 99 (6), pp. 3445–3455, 1996.

[6] P. D. Wilcox, “Array imaging of noisy materials,” AIP Conf. Proc., vol. 1335, pp. 890–897, 2011.

[7] T. S. Barber, P. D. Wilcox, and A. D. Nixon, “Optimization of element length for imaging small volumetric reflectors with linear ultrasonic arrays”, AIP Conf. Proc., vol. 1706, 020016, 2016.

[8] A. Velichko, “Quantification of the effect of multiple scattering on array imaging performance,” IEEE Trans. Ultrason., Ferroelectr., Freq. Control, vol. 67, no. 1, pp. 92–105, Jan. 2020.

[9] A. Van Pamel, P. B. Nagy and M. J. S. Lowe, “On the dimensionality of elastic wave scattering within heterogeneous media”, J. Acoust. Soc. Am. 140 (6), pp.4360-4366, 2016.

[10] A. Velichko, L. Bai, and B. W. Drinkwater, “Ultrasonic defect characterization using parametric-manifold mapping,” Proc. Roy. Soc. A, vol. 473, no. 2202, Jun. 2017, 20170056.

[11] A. Velichko and P. D. Wilcox, “Reversible back-propagation imaging algorithm for postprocessing of ultrasonic array data,” IEEE Trans. Ultrason., Ferroelectr., Freq. Control, vol. 56, no. 11, pp. 2492–2503, Nov. 2009.

[12] A. Velichko and P. D. Wilcox, “An analytical comparison of ultrasonic array imaging algorithms,” J. Acoust. Soc. Amer., vol. 127, no. 4, pp. 2377–2384, Apr. 2010.

[13] P. D. Wilcox and J. Zhang, “Quantification of the effect of array element pitch on imaging performance,” IEEE Trans. Ultrason., Ferroelectr., Freq. Control, vol. 65, no. 4, pp. 600–616, Apr. 2018.

[14] F. J. Margetan, R. B. Thompson, and I. Yalda-Mooshabad, “Backscattered microstructural noise in ultrasonic toneburst Inspections”, Journal of Nondestructive Evaluation, Vol. 13, No. 3, pp. 111-136, 1994.

[15] K. Y. Han and R. B. Thompson, ‘‘Ultrasonic Backscattering in Duplex Microstructures: Theory and Application to Titanium Alloys,’’ Metall. Trans., vol. 28A, pp. 91-104, Jan. 1997.

[16] R. B. Thompson, *et. al.*, “Scattering of elastic waves in simple and complex polycrystals”, Wave Motion, 45, pp. 655–674, 2008.

[17] Y. Liu, *et. al.*, “Can ultrasound attenuation measurement be used to characterise grain statistics in castings?”, Ultrasonics, 115, (2021), 106441.

[18] P. D. Panetta, L. Bland, and M. Tracy, “Ultrasonic characterization of blisk and disk gradient microstructures to improve fatigue life and creep resistance”, U.S. Department of Transportation, Federal Aviation Administration, report DOT/FAA/TC-13/35, 2013.

[19] S.I. Rokhlin, G. Sha, J. Li, A. L. Pilchak, “Inversion methodology for ultrasonic characterization of polycrystals with clusters of preferentially oriented grains”, Ultrasonics, 115, (2021), 106433.

[20] P. B. Nagy, L. Adler, “Scattering induced attenuation of ultrasonic backscattering”, In: Thompson D.O., Chimenti D.E. (eds) Review of Progress in Quantitative Nondestructive Evaluation. Springer, Boston, MA., pp. 1263-1271, 1988.

[21] V. Dorval, “Accounting for Structural Noise and Attenuation in the Modeling of the Ultrasonic Testing of Polycrystalline Materials”, AIP Conference Proceedings 1211, 1309 (2010).

  